

Correlation Between Resistance to Carburization and Resistance to Oxidation of Selected High-Temperature Alloys

H. M. Tawancy

Received: 1 September 2014 / Revised: 27 October 2014 / Published online: 6 November 2014
© Springer Science+Business Media New York 2014

Abstract It is shown that a one-to-one correspondence exists between the resistance to carburization and resistance to oxidation of selected Cr_2O_3 - and Al_2O_3 -forming alloys as determined from carburization and oxidation tests. Although the Cr_2O_3 -forming alloys are unable to maintain protective scales in an environment characterized by low oxygen potential and high carbon activity, the kinetics of carburization are found to be functions of the exact chemical composition. Ingress of carbon can lead to precipitation of carbides, particularly those based upon the Cr_7C_3 and Cr_{23}C_6 compositions with the latter enhancing the precipitation of CrFe sigma phase. In contrast, an Al_2O_3 -forming alloy with balanced Ni, Cr and Al contents is found to have superior resistance to carburization due to: (i) formation of highly protective Y-modified oxide, and (ii) higher solubility of C. It is concluded that Al_2O_3 -forming alloys can have a great deal of potential in applications requiring high resistance to carburization.

Keywords Carburization · Oxidation · Cr_2O_3 scale · Al_2O_3 scale · Electron microscopy

Introduction

Many petrochemical processes involve chemical reactions of carbonaceous gases, e.g. methane (CH_4), at high temperatures in the vicinity of 900 °C, which release free carbon. Examples of such processes include the production of ethylene, methanol and hydrogen [1]. Interaction between carbon and the materials used to manufacture various components particularly furnace tubes is a mode of high

H. M. Tawancy (✉)

Center for Engineering Research, Research Institute, King Fahd University of Petroleum and Minerals, P. O. Box 1639, Dhahran 31261, Saudi Arabia
e-mail: tawancy@kfupm.edu.sa

temperature corrosion referred to as carburization [1–6]. Commonly, two classes of engineering alloys are used in those applications: (i) heat-resistant steel castings such as the HP and HK grades [7–14], and (ii) wrought Fe-based superalloys particularly 310 stainless steel and alloy 800H [14–23]. Both classes are based upon the Fe–Cr–Ni system and rely upon a surface layer of Cr_2O_3 -based scale for environmental protection [2–5].

Carburization results in precipitation of various types of Cr-rich carbides, which can degrade both the environmental resistance and mechanical strength of the component. The problem can be compounded by forming an adherent surface layer of coke, which acts as thermal insulator requiring higher temperature to maintain the process, which accelerates the carburization rate as well as creep damage. In this case, a decoking process is carried out at regular intervals where the hydrocarbon feed is shut off and both steam and water are passed through the system. Some of the coke is burned away and some is cracked off the surface and blown away. Since the component is subjected to severe thermal shock during the decoking process, the useful life of the component can be shortened by increasing the decoking cycles.

An example is given in Fig. 1 to illustrate the damage produced in a furnace tube made of HK40 steel and used in the production of ethylene. Usually these tubes are designed for a service life of 100,000 h [1]. However, in the example of Fig. 1, the damage has occurred after about 22,000 h, which is reflected by sagging of the tube due to deposition of coke (Fig. 1a) as well as the development of through the thickness longitudinal crack (Fig. 1b, c). An adherent layer of coke at the inner tube surface is shown in Fig. 1d.

Typically, the environment encountered in the above petrochemical processes is reducing and characterized by low oxygen potential and high carbon activity. It is then expected that the ability of the structural material to develop and maintain a protective oxide scale plays a key role in determining the useful service life of the component. Specifically, the oxide layer must act as an effective barrier toward inward diffusion of carbon. Therefore, many studies have focused on the compositional parameters, which influence the susceptibility to carburization attack through their effect on oxidation behavior. A number of studies have demonstrated that carburization resistance is improved by increasing the Cr and Ni contents [7, 24–27]. In contrast, it is suggested in another study that carburization resistance is a more sensitive function of the Cr content rather than the Ni content [17]. Since Cr and Fe are the major carbide-forming elements and Ni is inert in Fe–Cr–Ni alloys, an earlier study shows that the resistance to carburization is improved by a factor of 3 as the $\text{Ni}/(\text{Cr} + \text{Fe})$ ratio is increased from 0.3 to 1, however, the exact effect may also be influenced by the concentrations of minor elements particularly Si, Al and Ti [15]. This has been confirmed in more recent studies demonstrating the beneficial effects of Si [28] as well as Si and Al [8]. The role of the protective oxide is also elucidated in various mechanisms proposed to explain the sequence of events leading to carburization attack [1, 12, 15, 29]. However, based upon some differences in the oxidation behavior of 310 stainless steel (nominal Cr and Ni contents of 25 and 20 wt% respectively) and alloy 800H (nominal Cr and Ni contents of 21 and 33 wt% respectively), it has been suggested that a higher

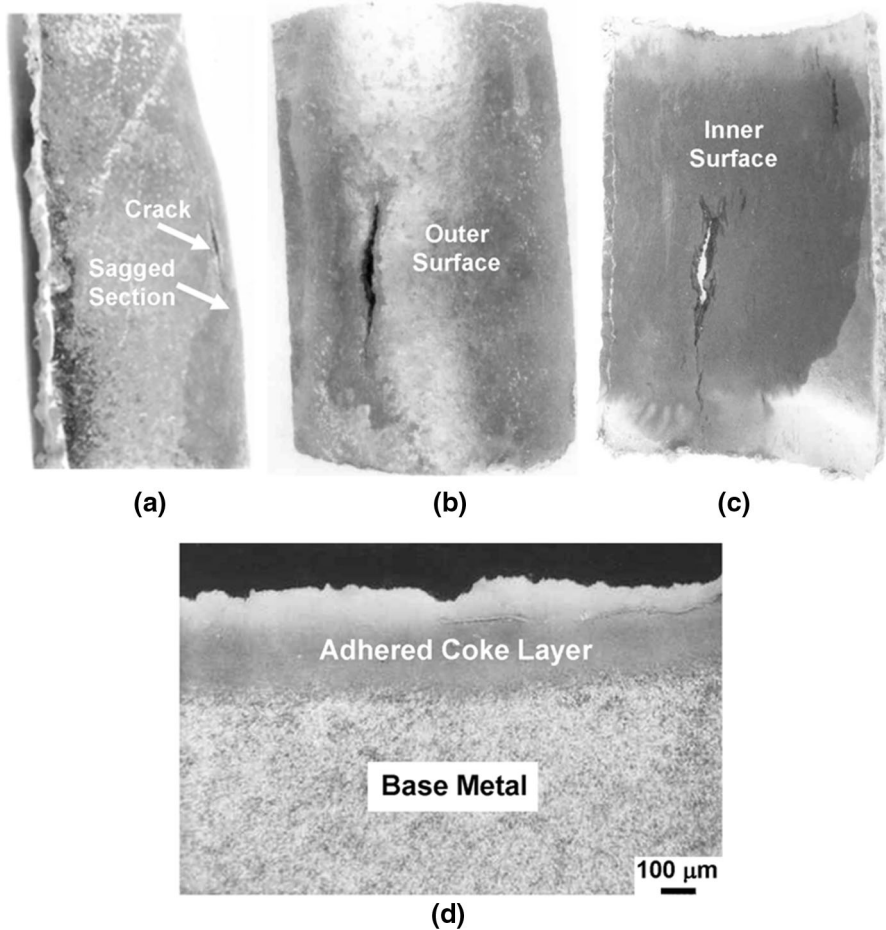


Fig. 1 An example illustrating the damage sustained by a furnace tube made of HK40 steel after about 22,000 h of exposure in a carburizing environment produced during ethylene production at a nominal temperature of 850 °C. **a** Sagging of the furnace tube due to coke deposition at the *inner wall*; a longitudinal crack is indicated by the *arrow*. **b** The crack as viewed from the *outer surface*. **c** The crack as viewed from the *inner surface*. **(d)** A low-magnification optical micrograph showing a layer of coke about 300 µm in thickness adhered to the inner surface of the tube

oxidation resistance may not necessarily imply a higher resistance to carburization [30].

It is evident from the previous studies that there are still some discrepancies regarding the role of protective oxide in carburization and in particular the influence of various alloying elements. Given the recognized effect of minor elements, one possible reason is that only nominal compositions of commercial alloys are given in most of the previous studies. On the other hand it is also possible that there is an optimum Cr content, which is most favorable for both oxidation and carburization. To elucidate the relationship between oxidation behavior and susceptibility to

carburization, the present study has been undertaken to compare the behavior of Cr_2O_3 - and Al_2O_3 -forming alloys. The study include: (i) heat resistant steel casting of the HP + Nb grade and the wrought INCOLOY[®] alloy 800H (INCOLOY is a registered trademark of the Special Metals Corporation Group of Companies) and 310 stainless steel representing Cr_2O_3 -forming alloys based upon the Fe–Cr–Ni system, and (ii) the wrought Ni-based HAYNES[®] alloy 214 (HAYNES is a registered trademark of the Haynes International Company) which is known for its superior oxidation resistance due to the formation yttrium-modified layer of Al_2O_3 [31].

Experimental Procedures

Table 1 lists the nominal chemical compositions of the alloys included in the study as well as the compositions of the samples used in the study as measured by inductively coupled plasma atomic emission spectroscopy (ICP-AES) with the exception of the carbon concentration, which was measured by combustion calorimetry [32]. All test specimens were prepared with a size of $25 \times 25 \times 3 \text{ mm}^3$. Prior to testing, all specimens were ground to 120 finish and then ultrasonically cleaned in acetone. Carburization was induced by exposure for up to 1,000 h at 870, 925 and 980 °C in an environment consisting of Ar-5 % CH₄-5 % H₂-5 % CO by volume. This environment is highly carburizing due to its low oxygen potential and high carbon activity (at 925 °C, the oxygen potential = 10^{-24} atm. and the carbon activity = 1) [33, 34]. Since the equilibrium dissociation pressures of Cr_2O_3 and Al_2O_3 at 925 °C are 2.6×10^{-23} and 4.5×10^{-38} atm respectively [3], the environment used in the study has an oxygen potential where Cr_2O_3 is unstable but Al_2O_3 is stable. A thermogravimetric unit was used to determine the kinetics of carburization of each alloy. From the observed weight changes, the temperature-dependent reaction rate constant (K) was calculated from the well known relationship: $(\Delta W/A)^2 = Kt$ where ΔW is the weight change, t is the exposure time at a given temperature and A is the surface area of the specimen. The respective activation energy was determined from the slope of $\ln K$ versus $1/T$ plots where T is the exposure temperature in degrees Kelvin. Comparative resistance to carburization was determined from the mass of carbon pickup (ΔC), which was determined from the measured carbon contents before and after testing. The results were expressed in mass pickup per unit area (Δm) mg/cm^2 using the equation: $\Delta m = \Delta C(W/A)$ where W is the weight of specimen before the test in mg and A is its surface area in cm^2 [30, 33].

To correlate the oxidation resistance with resistance to carburization, static oxidation tests were carried by exposing specimens in air for 1,000 h at 925 °C. Oxidized specimens were optically examined to determine the average metal affected (metal loss + internal penetration) according to ASTM G54-77 specifications (recommended standard practice for simple oxidation testing) [35].

Detailed microstructural characterization of carburized specimens was carried out using scanning electron microscopy (SEM) combined with energy dispersive X-ray spectroscopy and transmission/scanning transmission electron microscopy

Table 1 Chemical compositions of the alloys investigated: nominal (measured) wt%

Element	310ss	800H	HP + Nb	214
Fe	Balance (51.86)	39.5 ^b (43.75)	Balance (32.68)	3 ^a (2.11)
Cr	24–26 (25.23)	19–23 (21.94)	24–28	14–18 (16.29)
Ni	19–22 (20.63)	30–35 (32.84)	30–37 (36.97)	Balance (76.70)
Nb			2.5 ^a (1.76)	
Al		0.15–0.60 (0.32)		4.5 ^a (4.37)
Ti		0.15–0.60 (0.36)		
Al + Ti		0.4–0 (0.68)		
Mn	2 ^a (1.42)	1.5 ^a (0.96)	2 ^a (1.69)	0.5 ^a (0.23)
Si	0.5 ^a (0.32)	1 ^a (0.75)	2 ^a (1.72)	0.2 ^a (0.12)
Y				0.01 ^a (0.08)
C	0.25 ^a (0.14)	0.08 ^a (0.04)	0.35–0.75 (0.58)	0.04–0.1 (0.06)
P	0.45 ^a (0.30)	0.03 ^a (0.02)	0.03 ^a (0.02)	0.03 ^a (0.02)
S	0.3 ^a (0.10)	0.03 ^a (0.02)	0.03 ^a (0.02)	0.03 ^a (0.02)

^a Maximum^b Minimum

(TEM/STEM) as well as X-ray diffraction using Cu-K α radiation. A Rigaku -PDXL software system was used for phase identification and the results were complemented by TEM/STEM analysis. Whenever applicable, etching in 10 % oxalic acid was used to reveal the gross grain structure. Thin-foils transparent to electron were prepared by electro-polishing in a solution consisting of 30 % nitric acid in methanol. For oxidized specimens, the oxide layer near the oxide-metal interface was revealed by first electro-polishing on the metal side until perforation occurred. and then the oxide films left behind were thinned in an ion beam mill [36]. All the foils were examined at an accelerating voltage of 200 keV and an electron probe diameter of 2 nm was used for microchemical analysis.

Results and Discussion

Dependence of Carburization Kinetics on Alloy Composition

Figure 2 shows the temperature dependence of the reaction rate constant on temperature in the range of 870–980 °C. The linear relationship is indicative of a reaction controlled by a parabolic rate law consistent with the results of earlier studies [14–16]. Table 2 lists the activation energy for each alloy as estimated from the slopes of the lines in Fig. 2. As can be seen the activation energy for the alloys based upon the Fe–Cr–Ni system ranges from about 137 kJ/mol for 310 stainless steel to 208 kJ/mol for HP + Nb steel with an intermediate value of 174 kJ/mol for alloy 800H. These values are consistent with a carburization reaction governed by diffusional transport of C through less protective carbide scale in the absence of protective oxide scales [14–16, 36] as confirmed by the results of microstructural characterization presented later.

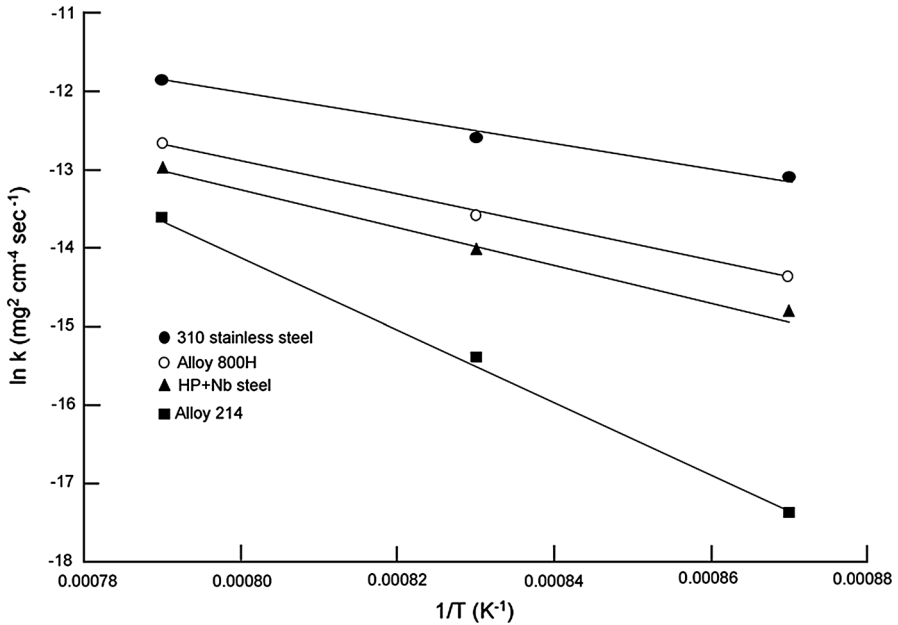


Fig. 2 Functional dependence of the carburization reaction rate constant K on temperature T of the alloys included in the study

Since Cr and Fe are the only carbide forming elements in Fe–Cr–Ni alloys, it is expected that the resistance to carburization can be improved by lowering their concentrations. However, since Cr is essential for adequate oxidation resistance, it is important to identify the concentration, which optimizes the resistance to both carburization and oxidation. Nickel is found to increase the solubility of C in the alloy matrix [37, 38] leaving more free Cr, which accelerates the kinetics of forming Cr_2O_3 [37]. Also, it has been reported that Ni improves the adhesion of Cr_2O_3 particularly in the presence of Fe [26, 27]. Although Si is known to improve the resistance to carburization of Fe–Cr–Ni alloys [15, 28], it is noted here that higher concentrations of Si can stabilize the detrimental laves phase in heat-resistant steels containing refractory elements such as Nb and W [39].

Figure 3 summarizes the functional dependence of carburization parameters of Fe–Cr–Ni alloys on their compositions. Figure 3a illustrates the functional dependence of the mass of carbon pickup after 1,000 h of exposure at 925 °C on the Ni/Cr + Fe ratio. It is observed that the mass of carbon pickup decreases from a value of about 14 mg/cm² for 310 stainless steel (Ni/Cr + Fe = 0.27) to 1.8 mg/cm² for HP + Nb steel (Ni/Cr + Fe = 0.65) with a value of 2.5 mg/cm² for alloy 800H (Ni/Cr + Fe = 0.51). As can be seen, the effect of the (Ni/Cr + Fe) ratio tends to level off for a ratio approaching 1. Also, a higher Ni/(Cr + Fe) ratio favors higher activation energy for carburization as shown in Fig. 3b. The beneficial effect of Si on the resistance to carburization is demonstrated in Fig. 3c.

Table 2 Activation energies

Alloy (kJ/mol)	Activation energy
310ss	137
800H	174
HP + Nb steel	208
214	385

In contrast with the Fe–Cr–Ni alloys, alloy 214 is found to have much higher activation energy of 385 kJ/mol as shown in Table 2., which is comparable to that characterizing oxidation of a number of Al₂O₃-forming alloys [40]. As shown below, alloy 214 is found to remain capable of developing and maintaining a protective Al₂O₃ scale in the carburizing environment employed in the present study.

Relationship Between Resistance to Carburization and Resistance to Oxidation

Figure 4 illustrates the carburization resistance of the alloys included in the study expressed in mass of carbon pickup after 1,000 h of exposure at 925 °C in comparison with oxidation resistance expressed as total metal affected after 1,000 h of exposure in air at 925 °C. A one-to-one correspondence is observed to exist between the resistance to carburization and resistance to oxidation with superior performance of alloy 214. It is observed that the total metal affected as well as the mass of carbon pickup corresponding to alloy 214 are one order of magnitude less those of alloys 800H and HP + Nb steel and two orders of magnitude less than those of 310 stainless steel.

Secondary electron SEM images and corresponding energy dispersive spectra illustrating the morphology and elemental composition of the surface scales developed by the Fe–Cr–Ni alloys after exposure for 1,000 h at 925 °C in air are shown in Fig. 5. As expected, each alloy can be seen to develop a Cr₂O₃-based scale with various concentrations of Fe and Ni. It is noted from Fig. 5a that the scale developed by HP + Nb steel is relatively more compact and has a finer structure in comparison with the scales developed by alloy 800H (Fig. 5c) and 310 stainless steel (Fig. 5e). Also, the scale of HP + Nb steel is observed to contain higher concentration of Si (Fig. 5b) due its higher Si content (Table 1). It is possible that Si is also present in the scales of alloys 800H (Fig. 5d) and 310 stainless steel (Fig. 5f) but in too small amounts to be detected by energy dispersive spectroscopy. Cracks are noted in the coarser scale developed by 310 stainless steel (Fig. 5e) which is also distinguished by higher concentration of Fe (Fig. 5f) in comparison with HP + Nb steel (Fig. 5b) and alloy 800H (Fig. 5d). This may be due to the presence of Fe₂O₃ in the scale and/or substitution of some Cr by Fe in the Cr₂O₃ scale. Evidently, the less protective scale developed by 310 stainless steel can explain its lowest resistance to carburization observed in Fig. 4b.

All Fe–Cr–Ni alloys included in the present study are found to develop a carbide scale rather than an oxide scale after exposure to the carburizing environment.

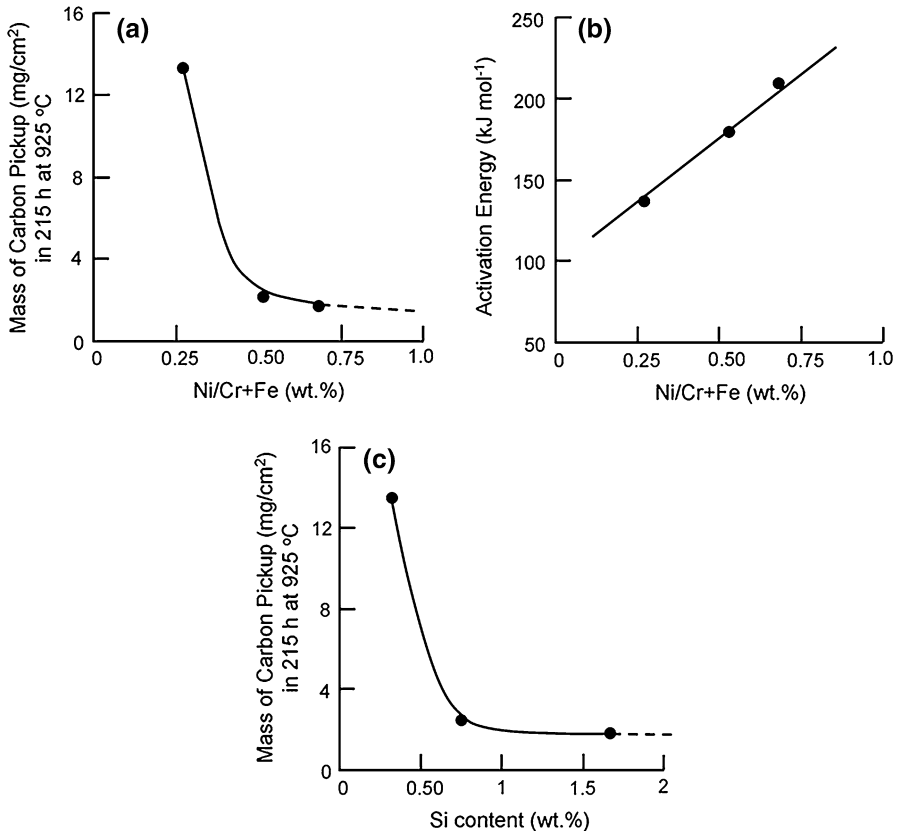


Fig. 3 Functional dependence of carburization kinetics on chemical composition of alloys based upon the Fe–Cr–Ni system. **a** Effect of Ni/(Cr + Fe) ratio in wt% on the mass of carbon pickup (1,000 h of exposure at 925 °C). **b** Effect of Ni/(Cr + Fe) ratio on activation energy. **c** Effect of Si content on mass of carbon pickup (1,000 h of exposure at 925 °C)

Occasionally, however, small islands of an oxide phase are observed beneath the carbide scale as shown later. As an example, Fig. 6 shows the morphology, elemental composition and the structure of the surface scale developed by HP + Nb steel after 1,000 h of exposure at 925 °C in the carburizing environment. As can be seen from the secondary electron SEM image of Fig. 6a and corresponding energy dispersive spectrum of Fig. 6b, the scale consists of Cr-rich carbide containing some Fe and a trace amount of Ni. Figure 6c shows a corresponding X-ray diffraction pattern where all observed reflections are indexed in terms of two carbide phases: (i) M_7C_3 with hexagonal structure ($a \approx 1.4$ nm, $c \approx 0.5$ nm)), and (ii) $M_{23}C_6$ with face-centered cubic structure ($a \approx 1.1$ nm) where M stands for the carbide-forming elements particularly Cr and Fe.

An example derived from 310 stainless steel to illustrate characteristic microstructure and composition of a carburized Fe–Cr–Ni alloy along a cross-section of the carbide scale and into the substrate is given in Fig. 7. As can be seen

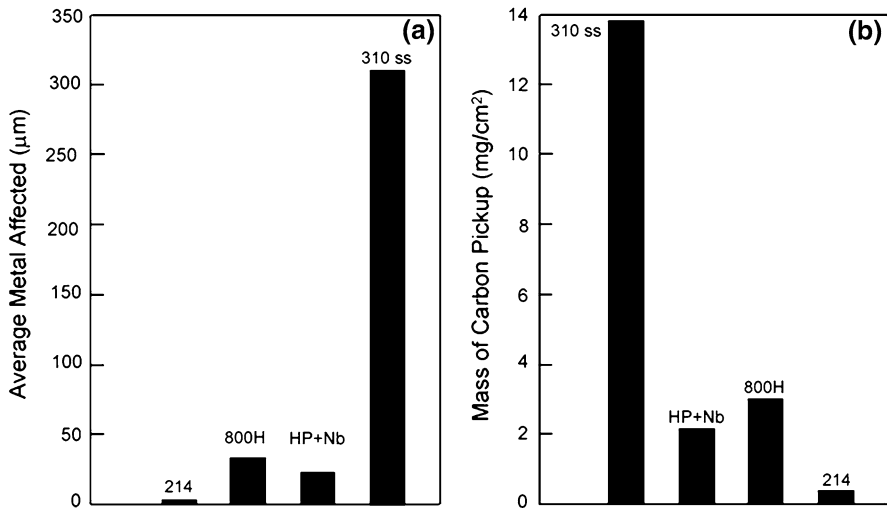


Fig. 4 Comparative oxidation and carburization resistance of the alloys included in the study. **a** Oxidation resistance as measured by the total metal affected after 1,000 h of exposure in air at 925 °C. **b** Carburization resistance as measured by the mass of carbon pickup after 1,000 h of exposure in the carburizing environment at 925 °C

from the backscattered electron image of Fig. 7a, the surface scale is followed by a precipitate-free zone and the alloy matrix, which contains high density of precipitates. As shown later, these precipitates are identified as a mixture of carbides and sigma phase. A precipitate-free zone such as that observed in Fig. 7a has been observed in other Fe–Cr–Ni alloys and is interpreted in terms of spallation and regeneration of Cr_2O_3 provided the Cr concentration near the surface remains to be at least 10 wt% [12]. It is evident from the energy dispersive spectra of Fig. 7b, c that the scale consists of Cr- and Fe-rich carbide with small islands of Cr-rich oxide indicating that the carbide phase has overgrown the oxide phase. The spectrum of Fig. 7d shows that the precipitate-free zone is depleted in Cr. This is further illustrated in Fig. 8, which shows a typical concentration profile of Cr across the scale and into the substrate shown in the image of Fig. 7a.

In contrast, with the case of the Cr_2O_3 -forming Fe–Cr–Ni alloys, alloy 214 has been able to develop and maintain a protective Al_2O_3 -based scale under conditions of low oxygen potential and high carbon activity as illustrated in Fig. 9. This behavior has also been reported for a mixed carburizing/oxidizing environment [40]. As can be seen from the secondary electron SEM image of Fig. 9a, the surface scale is compact and has a fine structure. The corresponding elemental composition shown in the energy dispersive spectrum of Fig. 9b is consistent with Al_2O_3 -based scale. Figure 9c is a backscattered electron SEM image along a cross-section of the very thin layer of the scale and into the alloy substrate. Evidently, the alloy has been able to accommodate the small amount of carbon picked up (Fig. 4b) in solid-solution without precipitation of carbide phases. This is further illustrated in the grain structure shown in the optical micrograph of Fig. 9d. As demonstrated below,

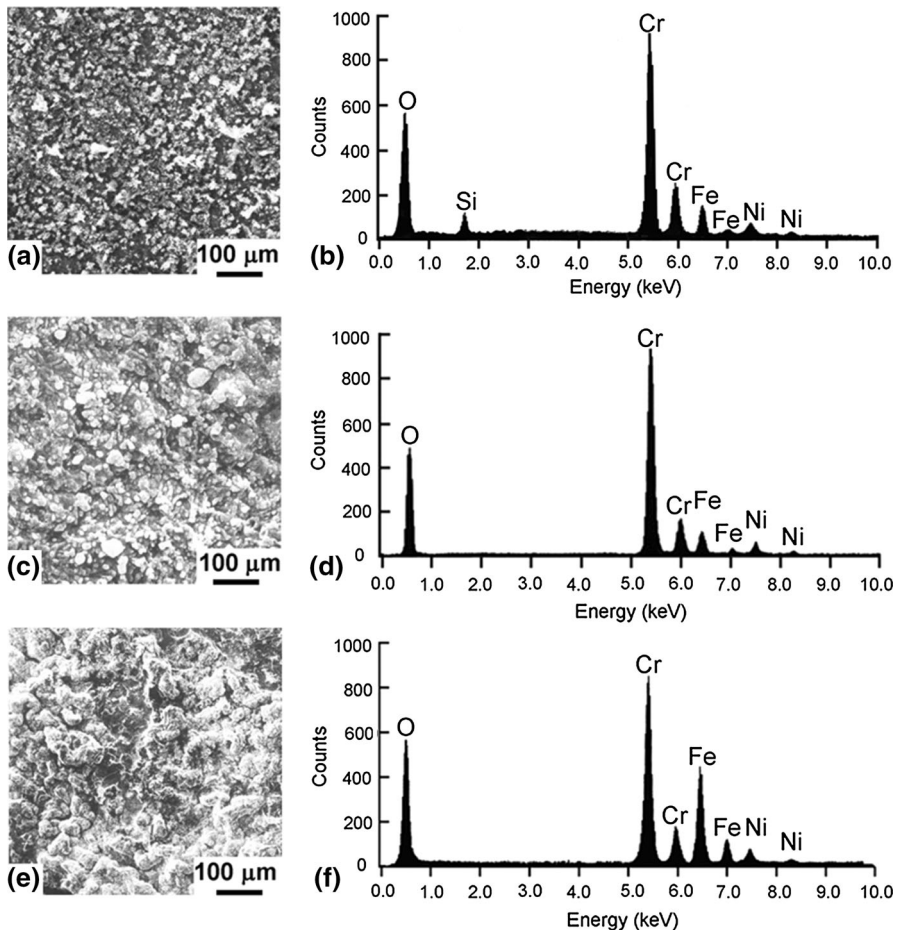


Fig. 5 Secondary electron SEM images and corresponding energy dispersive X-ray spectra illustrating the morphology and elemental composition of the surface oxide developed by the alloys based upon the Fe–Cr–Ni system after 1,000 h of exposure in air at 925 °C. **a** Oxide morphology of HP + Nb steel. **b** Corresponding elemental composition. **c** Oxide morphology of alloy 800H. **d** Corresponding elemental composition. **e** Oxide morphology of 310 stainless steel. **f** Corresponding elemental composition

the distinctive behavior of alloy 214 can also be related to the beneficial effects of Y on its oxidation resistance.

Figure 10 summarizes the microstructural features of the Al_2O_3 layer in contact with alloy 214 as viewed on the fine scale of TEM and STEM. A bright-field TEM image illustrating the grain structure of Al_2O_3 is shown in Fig. 10a. It is observed that most of the grains assume a size on the nanoscale (<100 nm). A corresponding ring diffraction pattern consistent with the hexagonal structure of α - Al_2O_3 ($a \approx 0.5$ nm, $c \approx 1.3$ nm) is shown in Fig. 10b. Figure 10c shows an energy dispersive X-ray spectrum derived from an oxide grain. As can be seen, the oxide contains a small concentration of Cr and trace amounts of Y and Ni. A

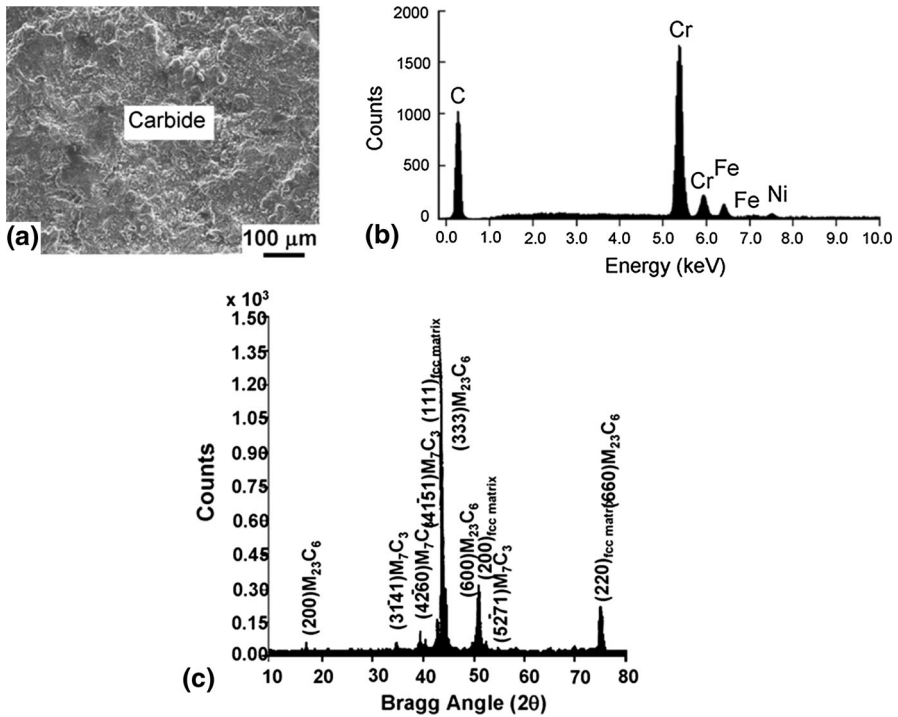


Fig. 6 Analysis of surface carbide scale formed on HP + Nb steel after 1,000 h of exposure at 925 °C in the carburizing environment. **a** Secondary electron SEM image illustrating the scale morphology. **b** Corresponding energy dispersive X-ray spectrum illustrating the elemental composition. **c** Corresponding X-ray diffraction pattern

concentration profile across a grain boundary of Al₂O₃ is shown in Fig. 10d and demonstrates the tendency of Y to segregate at grain boundaries of the oxide. Also, it is evident that a smaller concentration of Y is present within the grains. The various beneficial effects of Y on the protective nature of Al₂O₃ have long been recognized as documented in many review articles [41–47]. Among these effects is that Y increases the activity of Al and thus reduces the amount required to develop and maintain a continuous oxide layer. Also, segregation of Y to grain boundaries can enhance the protective nature of Al₂O₃ scale by: (i) filling pores and voids at the boundaries, which improves the cohesive strength of the scale, (ii) maintaining a fine-grained structure with improved high-temperature mechanical strength), and (iii) restricting short-circuit diffusion of oxygen along grain boundaries, which maintains a thin tenacious layer of scale minimizing the detrimental effects of growth stresses. The presence of some Y in solid-solution within the grains can decelerate the kinetics of Al lattice diffusion, which further contributes to maintaining a thin protective layer of scale. Therefore, the Y-modified Al₂O₃ scale can be expected to provide an effective barrier toward diffusional transport of C into the alloy. Based upon the above observations, it is

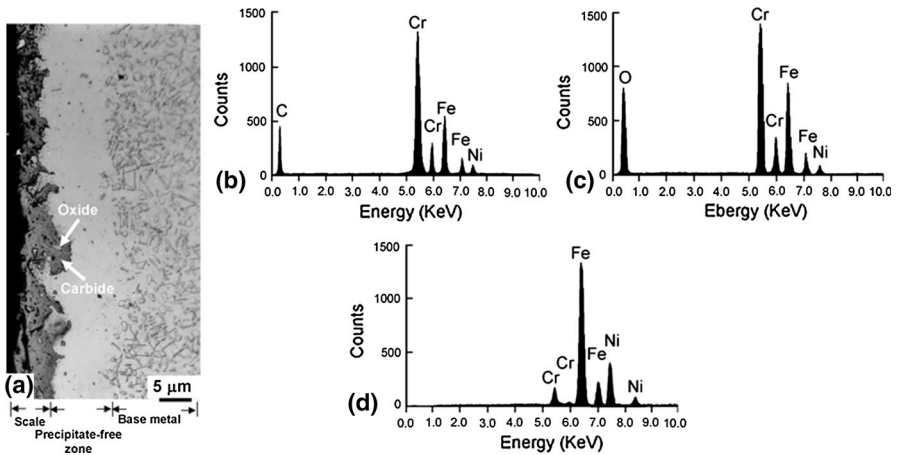


Fig. 7 An example derived from 310 stainless steel to illustrate the microstructure and composition along a cross-section of the scale and into the substrate after 215 h of exposure at 925 °C in the carburizing environment. **a** Backscattered electron composition image showing three distinct zones. **b** Energy dispersive X-ray spectrum illustrating the elemental composition of the carbide scale as indicated by the arrow in (a). **c** Energy dispersive X-ray spectrum illustrating the elemental composition of the oxide beneath the carbide scale as indicated by the arrow. **d** Energy dispersive X-ray spectrum illustrating the elemental composition of the precipitate-free zone

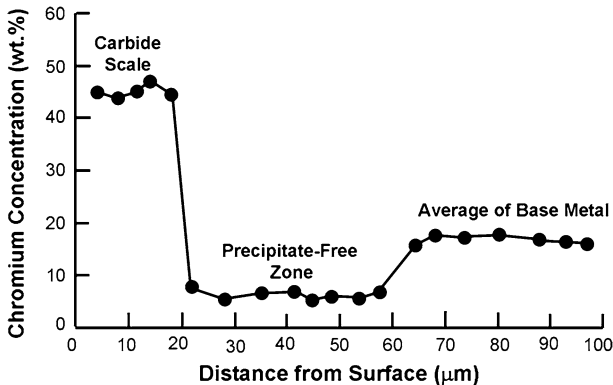


Fig. 8 Concentration profile of Cr along the cross-section of Fig. 7a showing the Cr content within the three zones

possible to correlate the superior performance of alloy 214 to three factors: (i) the highly protective nature of the Y-modified Al_2O_3 scale, (ii) the high Ni content, which increases the solubility of C [37, 38], and (iii) the lower content of carbide-forming elements particularly Cr. Evidently, the Al_2O_3 -forming alloy 214 follows the same behavior of Fe–Cr–Ni alloys regarding the effect of Ni/(Cr + Fe) ratio on the resistance to carburization.

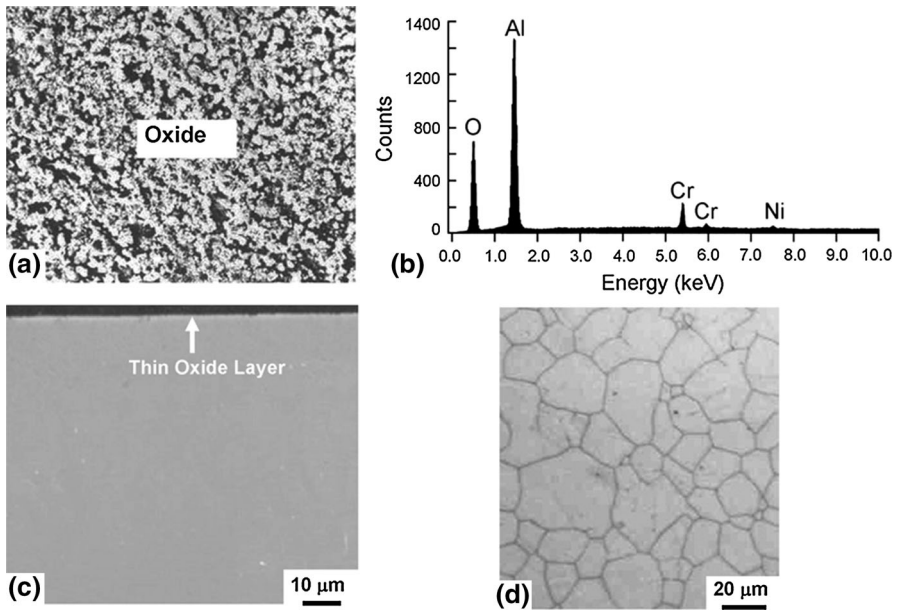


Fig. 9 Analysis of the scale developed by alloy 214 after 1,000 h of exposure at 925 °C in the carburizing environment. **a** Secondary electron SEM image illustrating the morphology of the surface scale. **b** Corresponding energy dispersive X-ray spectrum illustrating the elemental composition. **c** Backscattered electron SEM image along a cross-section of the scale and into the alloy. **d** Backscattered electron SEM image illustrating the grain structure

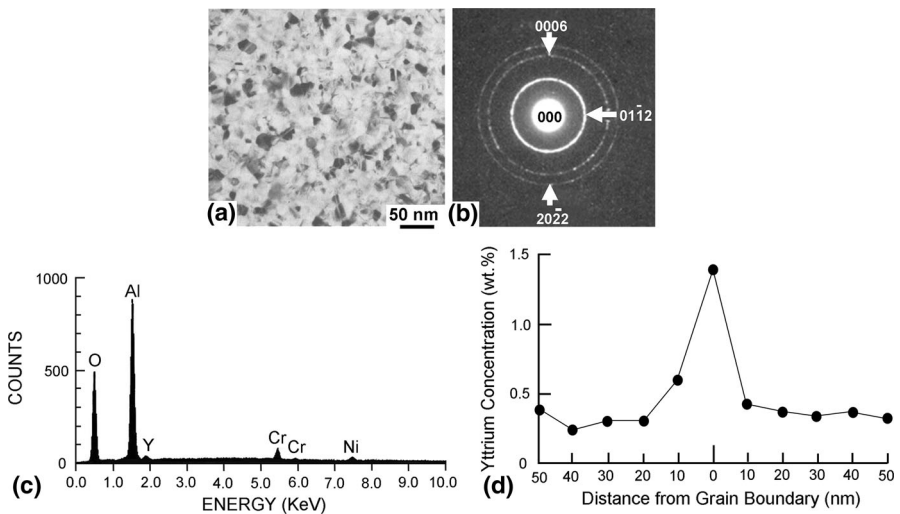


Fig. 10 Microstructural features of Al_2O_3 developed by alloy 214 after 1,000 h of exposure at 925 °C in air. **a** Bright-field TEM image illustrating the grain structure of the oxide. **b** Corresponding electron diffraction pattern indexed in terms of the hexagonal structure of $\alpha-Al_2O_3$. **c** Energy dispersive X-ray spectrum derived from a grain of Al_2O_3 . **d** Concentration profile of Y across a grain boundary of Al_2O_3

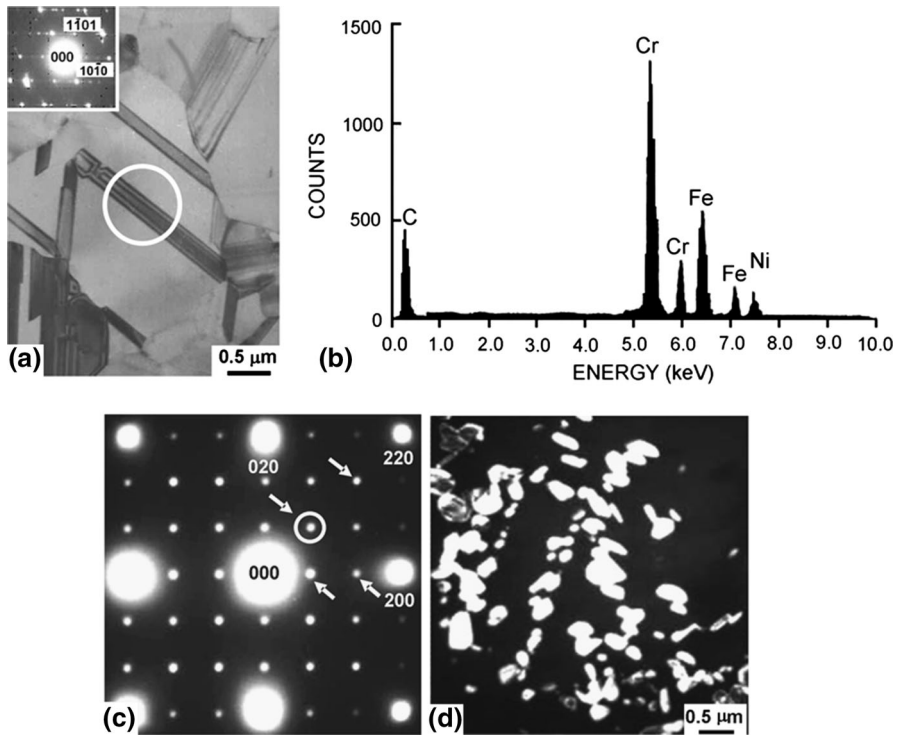


Fig. 11 Analysis of carbide precipitates in HP + Nb steel after 1,000 h of exposure at 925 °C in the carburizing environment. **a** Bright-field STEM image of M_7C_3 carbide particles; the *inset* is a microdiffraction pattern derived from the encircled region and indexed in terms of the hexagonal structure of the carbide. **c** Energy dispersive X-ray spectrum illustrating the elemental composition of the carbide consistent with $(Cr,Fe)_7C_3$ composition. **d** $(001)_{fcc}$ diffraction pattern showing characteristic $M_{23}C_6$ reflections at every one-third position of the fundamental fcc reflections. **e** Dark-field TEM image formed with the encircled reflection in **(d)** and showing carbide particles within the matrix phase

Effect of Carburization on Microstructure of Alloys Based Upon the Fe–Cr–Ni System

The most significant effect of carburization on the microstructures of HP + Nb steel, alloy 800H and 310 stainless steel is the precipitation of various amounts of carbide phases. Both the $(Cr,Fe)_3C_7$ - and $(Cr,Fe)_{23}C_6$ -types are identified in each of the three alloys. Examples of the two carbides as identified by TEM/STEM in HP + Nb steel are given in Fig. 11. Figure 11a shows a bright-field STEM image and corresponding micro diffraction pattern consistent with $[1\bar{1}\bar{2}1]$ orientation of the hexagonal structure of $(Cr,Fe)_7C_3$ ($a = 1.4$ nm, $c = 0.5$ nm). It is well known that the microstructure of this carbide is distinguished by high density of planar defects including twins and stacking faults [48] as observed in Fig. 11a. The corresponding elemental composition is shown in the energy dispersive spectrum of Fig. 11b, which is consistent with a Cr- and Fe-rich carbide phase. Figure 11c shows an electron diffraction pattern in $[001]$ orientation of the face-centered cubic (fcc)

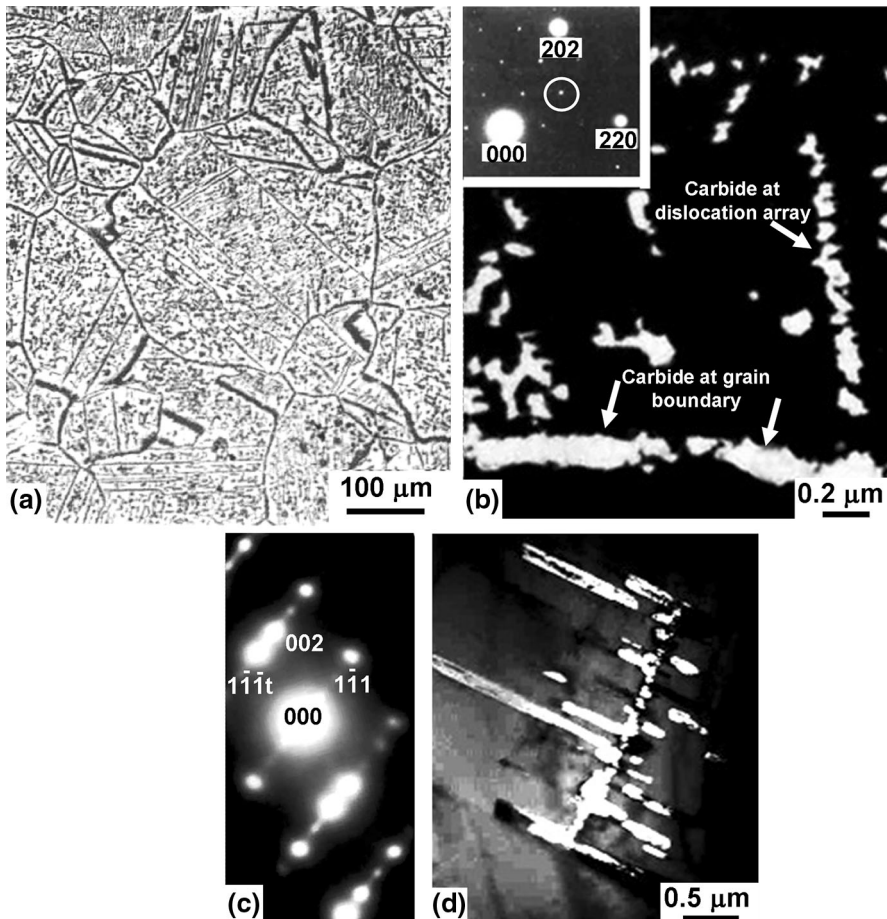


Fig. 12 Analysis of carbide precipitates in alloy 800H after 1,000 h of exposure at 925 °C in the carburizing environment. **a** Backscattered electron SEM image showing carbide precipitates throughout the grain structure. **b** Dark-field TEM image formed with the encircled $1/3 \langle 422 \rangle_{fcc}$ reflection and showing $M_{23}C_6$ carbide precipitates at a grain boundary as well as at an array of dislocations. **c** Twinned diffraction pattern in $\langle 110 \rangle_{fcc}$ orientation. **d** Dark-field image formed with the $[1]$ twin reflection in (c) and showing $M_{23}C_6$ carbide precipitates

structure of the austenitic matrix phase. A dark-field TEM image formed with the encircled $1/3 \langle 220 \rangle$ reflection in Fig. 11c is shown in Fig. 11d. Discrete particles are observed throughout the matrix phase. The diffraction pattern in Fig. 11c with fundamental fcc reflections and extra weaker reflections at every one-third position is typical of $M_{23}C_6$ -type carbide (M stands for metal), which is well known to have a lattice parameter about three times that of the matrix phase [48].

Figure 12 illustrates the carbide precipitates observed in alloy 800H. A backscattered electron SEM image illustrating the gross grain structure is shown in Fig. 12a. Precipitates are observed throughout the matrix and at grain boundaries. A dark-field TEM image and corresponding diffraction pattern near $\langle 111 \rangle_{fcc}$

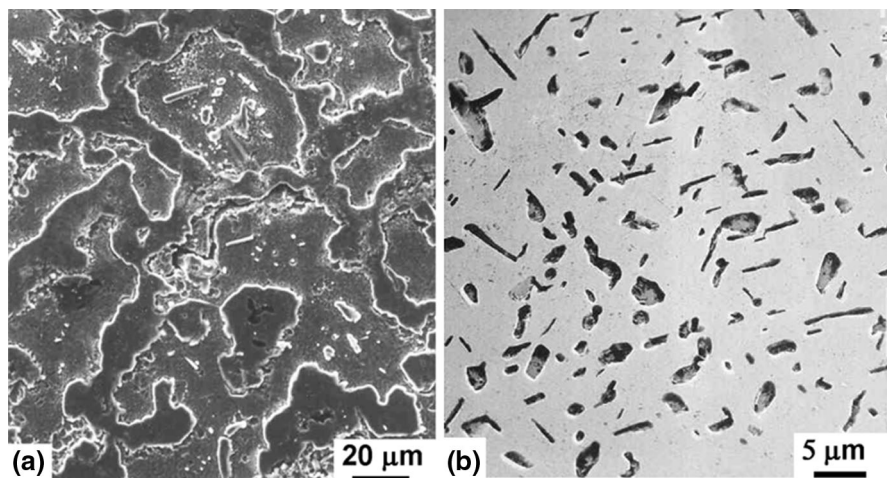


Fig. 13 Precipitates observed in 310 stainless steel after 1,000 h of exposure at 925 °C in the carburizing environment. **a** Secondary electron SEM image showing massive network of carbide at grain boundaries; fine precipitates assuming platelet morphology are observed with the grains. **b** Bright-field STEM image showing the precipitates with platelet morphology attached to discrete particles within the austenitic matrix phase

orientation illustrating $(\text{Cr,Fe})_{23}\text{C}_6$ carbide precipitates at a grain boundary and at an array of matrix dislocations are shown in Fig. 12b. Precipitates of the carbide at twin boundaries within the matrix phase are illustrated in the $\langle 110 \rangle$ twinned diffraction pattern and corresponding dark-field image of Fig. 12c, d respectively. It is known that the preferred nucleation sites for the M_{23}C_6 carbide include dislocations, twin boundaries and grain boundaries [49–51].

A distinctive feature of 310 stainless steel has been the observation of massive networks of carbide precipitates at grain boundaries as shown in the example of Fig. 13. A secondary electron SEM image illustrating the gross carbide morphology is shown in Fig. 13a. Small platelets are also observed within the matrix phase. A higher resolution bright-field STEM image of the matrix precipitates is shown in Fig. 13b. Fine platelets attached to discrete particles can be distinguished. An example illustrating the results of analyzing the nature of these precipitates is given in Fig. 14. A bright-field STEM image showing a platelet emanating from a discrete particle is shown in Fig. 14a and marked 1 and 2 respectively. Figure 14b illustrates an energy dispersive X-ray spectrum and microdiffraction pattern in [011] orientation derived from the platelet marked 1 in Fig. 14a. Both the spectrum and microdiffraction pattern are consistent with CrFe sigma phase with tetragonal structure ($a \approx 0.9$ nm, $c \approx 0.5$ nm). The discrete particle marked 2 in Fig. 14a is identified as $(\text{Cr,Fe})_{23}\text{C}_6$ carbide as illustrated in the spectrum of Fig. 14c and corresponding [112] microdiffraction pattern showing the characteristic carbide reflections at every one-third positions of the fundamental fcc reflections. It is well known that pre-precipitation of M_{23}C_6 carbide can promote the precipitation of sigma phase by acting as a preferred nucleation site [52].

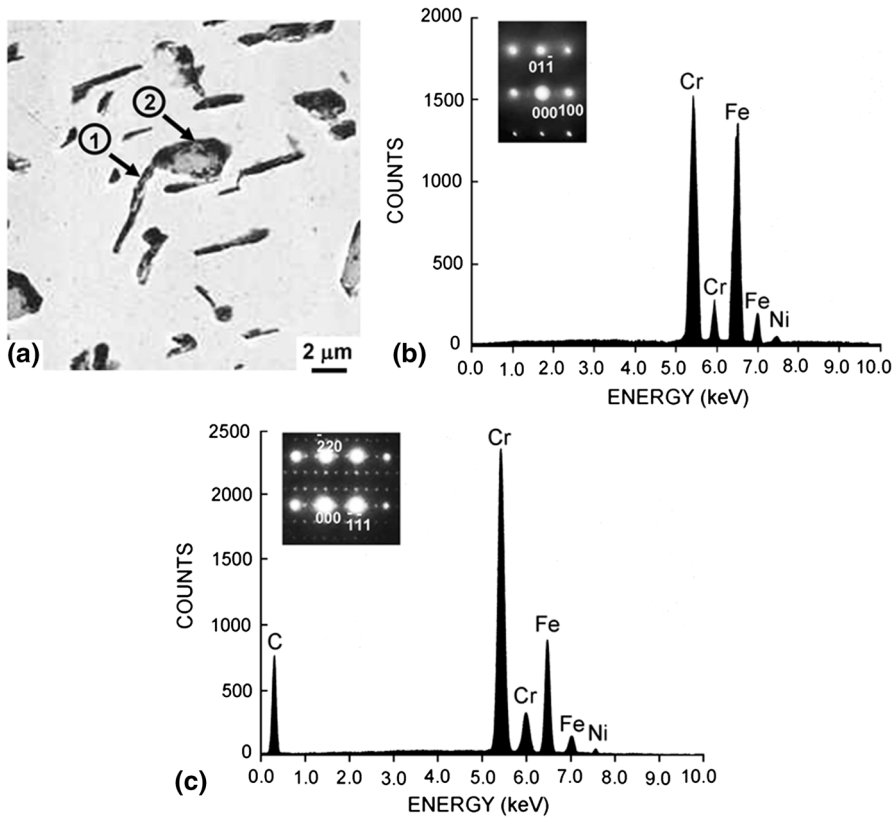


Fig. 14 Identification of the precipitates observed in Fig. 13b. **a** A high magnification image of the matrix precipitates. **a** Energy dispersive X-ray spectrum and corresponding microdiffraction pattern derived from the platelet marked 1 in (a) consistent with CrFe sigma phase with tetragonal structure. **b** Energy dispersive X-ray spectrum and corresponding microdiffraction pattern derived the particle marked 2 in (a) and consistent with $(\text{Cr,Fe})_{23}\text{C}_6$ carbide with cubic structure

Conclusions

It is concluded from this study that a one-to-one correspondence exists between the resistance to carburization and resistance to oxidation. Alloys with most protective oxide scale exhibit the highest resistance to carburization in an environment characterized by low oxygen potential and high carbon activity. The resistance to carburization of alloys based upon the Cr_2O_3 -forming Fe–Cr–Ni system is enhanced with increasing the Ni/(Cr + Fe) ratio well as the Si content. However, the respective beneficial effects are leveled off for a Ni/(Cr + Fe) ratio of about 1 in wt%. Carburization of these alloys results in precipitation of $(\text{Cr,Fe})_3\text{C}_7$ and $(\text{Cr,Fe})_{23}\text{C}_6$ carbides at grain boundaries as well as in the matrix phase. However, the resistance to carburization of the alloys based upon the Fe–Cr–Ni system is outperformed by an Al_2O_3 -forming alloy based upon the Ni–Cr–Al system with a critical addition of Y. Due to the higher Ni content and lower Cr content, the alloy

becomes more stable toward precipitation of carbide phases. An additional benefit is provided by the yttrium, which improves the protective nature of Al_2O_3 scale, which becomes an effective barrier toward the ingress of carbon into the alloy. Therefore, alloys protected by Al_2O_3 with balanced concentrations of Ni and carbide forming elements particularly Cr such as alloy 214 can offer better choice for applications where high resistance to carburization is required.

Acknowledgments It is a pleasure to acknowledge the continued support of King Fahd University of Petroleum and Minerals.

References

1. J. F. Norton, *Carburization in High Temperature Process Plant Materials* (Commission of the European Community Report No. EUR 7773, Luxembourg 1981).
2. C. M. Chun, S. Desai, F. Hershkowitz and T. A. Ramanarayanan, *Mater and Corrosion* **65**, 281 (2014).
3. G. Y. Lai, *High Temperature Corrosion and Materials Applications*, (ASM International, Materials Park, OH, 2007), p. 97.
4. G. Y. Lai, *High-Temperature Corrosion of Engineering Alloys*, (ASM International, Materials Park, OH, 1990), p. 47.
5. H. J. Grabke, *Materiali in Technologiae* **36**, 297 (2002).
6. J. Grabke, *Craburization: A High Temperature Corrosion Phenomenon* (Elsevier Science and Technology, Amsterdam, 1998) p. 3.
7. L. M. Shen, J. M. Gong and H. S. Liu, *Materials at High Temperature* **31**, 148 (2014).
8. J. Yan, Y. Gao, F. Yang, Y. Bai, Y. Liu, C. Yao, S. Hou and G. Liu, *Corrosion Science* **67**, 161 (2013).
9. L. H. de Almeida and A. F. Ribeiro, I.L. May. *Materials Characterization* **49**, 219 (2003).
10. X. Q. Wu, H. M. Jing, Y. G. Zheng, Z. M. Yao, W. Ke and Z. Q. Hu, *Materials Science and Engineering A* **293**, 252 (2000).
11. R. Petkovic-Luton and T. A. Ramanarayanan, *Oxidation of Metals* **34**, 381 (1990).
12. T. A. Ramanarayanan, R. Petkovic-Luton, J. D. Munford and A. Ozecin, *Material and Corrosion* **49**, 226 (1998).
13. G. M. Smith, D. J. Young and D. L. Trimm, *Oxidation of Metals* **18**, 229 (1982).
14. J. F. Norton, L. Blidegn, S. Canetoli and P. D. Frampton, *Werkstoffe und Korrosion* **32**, 467 (1981).
15. A. Schnaas and H. J. Grabke, *Oxidation of Metals* **12**, 387 (1978).
16. R. Yin, *Materials at High Temperatures* **21**, 205 (2004). 800H, 310.
17. R. Yin, *Corrosion and Science* **47**, 1896 (2005).
18. R. Yin, *Materials Science and Engineering A* **391**, 19 (2005).
19. R. C. Yin, I. M. Allam and A. Al-Farayedhi, *Oxidation of Metals* **60**, 315 (2003).
20. P. J. Smith, O. Vanderbiest and J. Corish, *Oxidation of Metals* **24**, 47 (1985).
21. P. J. Smith, O. Vanderbiest and J. Corish, *Oxidation of Metals* **24**, 277 (1985).
22. W. F. Chu and A. Rhamel, *Oxidation of Metals* **15**, 331 (1981).
23. Y. Nishiyama and N. Otsuka, *Corrosion* **61**, 84 (2005).
24. Y. Nishiyama, N. Otsuka and T. Nishizawa, *Corrosion* **59**, 688 (2003).
25. R. F. A. Pettersson, J. Enecker and L. Liu, *Materials at High Temperature* **22**, 269 (2005).
26. R. Peraldi and B. A. Pint, *Oxidation of Metals* **61**, 463 (2004).
27. T. D. Nguyen, J. Zhang and D. J. Young, *Oxidation of Metals* **81**, 549 (2014).
28. H. M. Tawancy and N. M. Abbas, *Journal of Material Science* **27**, 1061 (1992).
29. M.F. Rothman, G.Y. Lai, M.M. Antony, A.E. Miller, in *Proceedings of the 9th International Congress on Metallic Corrosion* (National Research Council, Canada 1984) pp. 66–72.
30. H. M. Tawancy and N. Sridhar, *Oxidation of Metals* **37**, 143 (1992).
31. F. Rouessac, A. Rouessac, *Chemical Analysis: Modern Instrumentation Methods and Techniques* (Wiley, Hoboken, NJ, 2007) p. 309 and 447.
32. G.Y. Lai, *High Temperature Corrosion in Energy Systems*, ed. M.F. Rothman (TMS-AIME, Warrendale, Pennsylvania 1985) p. 564.

33. G.Y. Lai, M.F. Rothman, *Corrosion 84* (NACE, Houston, TX, 1984) paper No. 11.
34. ASTM G54-84, Standard Practice for Simple Oxidation Testing (1996).
35. P. J. Goodhew, *Specimen Preparation for Transmission Electron Microscopy of Materials*, (Oxford University Press, Oxford, 1984), p. 21.
36. J. M. Harrison, J. F. Norton and R. T. Derricott, *Materials and Corrosion. Werkst. Korros.* **30**, 785 (1979).
37. K. Natesan and T. F. Kassner, *Metallurgical Transaction* **4**, 2557 (1973).
38. J. C. Greenbank, *The Journal of the Iron and Steel Institute* **210**, 111 (1970).
39. H. M. Tawancy and N. M. Abbas, *Journal of Materials Science* **40**, 2085 (2005).
40. I. M. Allam, *Oxidation of Metals* **72**, 127 (2007).
41. T. A. Ramanarayanan, R. A. Ayer, R. Petkovic-Luton and D. P. Leta, *Oxidation of Metals* **29**, 445 (1988).
42. G.C. Wood, F.H. Stott, in *High Temperature Corrosion*, ed. R.A. Rapp (NCE-6, Houston, Texas, 1983) p. 227.
43. H. Hindam and D. P. Whittle, *Oxidation of Metals* **18**, 245 (1982).
44. A.M. Huntz, in *The Role of Active Elements in the Oxidation Behavior of Metals and Alloys*, ed. E. Lang (Elsevier Applied Science, London, 1989), p. 81.
45. A. M. Huntz, *Materials Science and Engineering* **87**, 271 (1987).
46. F. H. Stott and G. C. Wood, *Materials Science and Engineering* **87**, 267 (1987).
47. D. P. Whittle and J. Stringer, *Philosophical Transactions of the Royal Society. London* **A295**, 309 (1980).
48. J. W. Edington, *Typical Electron Microscope Investigations*, (N.V. Philips, Eindhoven, 1976), p. 33.
49. J. B. Mitchell, *Metallography* **8**, 5 (1975).
50. F. R. Beckitt and B. R. Clark, *Acta Materialia* **15**, 113 (1967).
51. M. H. Lewis and B. Hattersley, *Acta Materialia* **13**, 1159 (1965).
52. G. Wallwork, J. Croll, in *Reviews of High Temperature Materials*, ed. J. Newkirk (Freund Publishing House, London, 1976) p. 69.